


In the format provided by the authors and unedited.

Dynamics and efficient conversion of excitons to trions in non-uniformly strained monolayer WS_2

Moshe G. Harats , Jan N. Kirchhof, Mengxiong Qiao, Kyrylo Greben  and Kirill I. Bolotin 

Department of Physics, Freie Universität Berlin, Berlin, Germany. ✉e-mail: kirill.bolotin@fu-berlin.de

Supplemental Materials: Dynamics and Efficient Conversion of Excitons to Trions in Non-Uniformly Strained Monolayer WS_2

Moshe G. Harats, Jan N. Kirchhof, Mengxiong Qiao, Kyrylo Greben, and Kirill I. Bolotin^{a)}
Department of Physics, Freie Universität Berlin, 14195 Berlin, Germany

I. EXPERIMENTAL SETUP

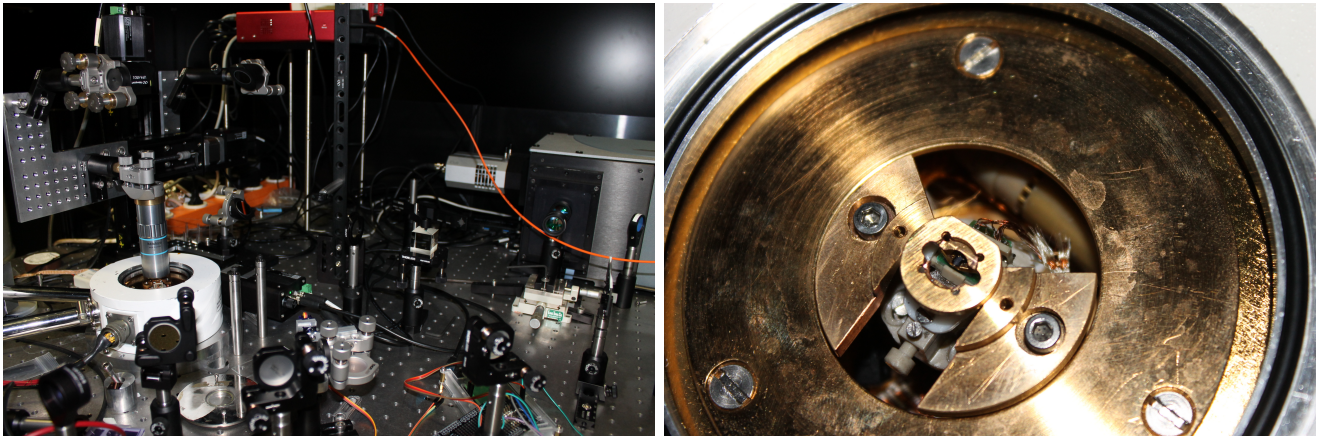
The experimental setup is depicted in Fig. 1(a) in the main text. A CW diode laser emitting at 532 nm (Thorlabs CPS532) is used. The laser passes through a beam-splitter cube, then it is aligned through a periscope to the sample. The periscope gives us the freedom to spatially scan the sample while maintaining the same focal spot and ensuring that the optical path for the photoluminescence (PL) is directed to an Andor spectrometer and CCD. The laser is focused onto the sample with a Mitutoyo PLAN APO HR 50X objective ($NA = 0.75$) and a notch filter is used to filter out the laser at the spectrometer entrance. Photos of the experimental setup are shown in Fig. S1.

The sample consists of a $150 \times 150\ \mu\text{m}^2$ Si/SiNx window (Norcada NX5015A) with a SiNx thickness of 50 nm . Holes with different diameters are defined using a focused beam of Gallium ions (Crossbeam 340 FIB) at 30 kV acceleration voltage and a current of 50 pA . We mechanically exfoliate WS_2 flakes from HQ Graphene onto a commercial PF X4 (6.5 mil) from Gel-Pak. The flake is verified as a monolayer using Raman and PL measurements (not shown). The flake is then transferred on top of the holes using a dry-transfer method^{S1}. An image of a complete sample is seen in Fig. 1(c) in the main text.

The sample is mounted underneath the objective, and it is approached from below using an Attocube piezo stack. The stack consists of steppers with 2.5 mm stepping range (ANPx51 for x,y stepping and ANPz51 for z stepping) and scanners (ANSxy50 for $35 \times 35\ \mu\text{m}^2$ x,y scan and ANPz51 for $5\ \mu\text{m}$ scan in the z direction). The piezo stack features full stepping range across the whole chip and enough distance between the tip and the mounted sample to avoid damage to the tip and the sample. To complete the AFM, we use piezo-resistive tips (SCL PRSA-L300-F50-Si-PCB)^{S2} mounted on a tunable angle ramp ($10^\circ - 30^\circ$). The electrical readout of the cantilever and the electrical input of the piezo scanners are connected to a Zurich Instrument MFLI lock-in amplifier with PLL and PID controllers. The PLL gives us frequency-locked tapping-mode capabilities. The PID controller enables scanning with the same AFM tip at amplitude-locked tapping mode and contact mode. The performance of the home-built AFM is shown in Fig. 1(d) in the main text.

II. NANOIDENTATION AND STRAIN CALCULATIONS

The theoretical derivation of the diffusion-drift model in the main text depends on the calculation of the strain profile, which in turn, is crucial for correct evaluation of the spatially-dependent band-gap under strain. To determine



(a) The full optical setup showing the periscope.

(b) The sample holder and the AFM tip inside the cryostat.

FIG. S1 Photos of the experimental setup.

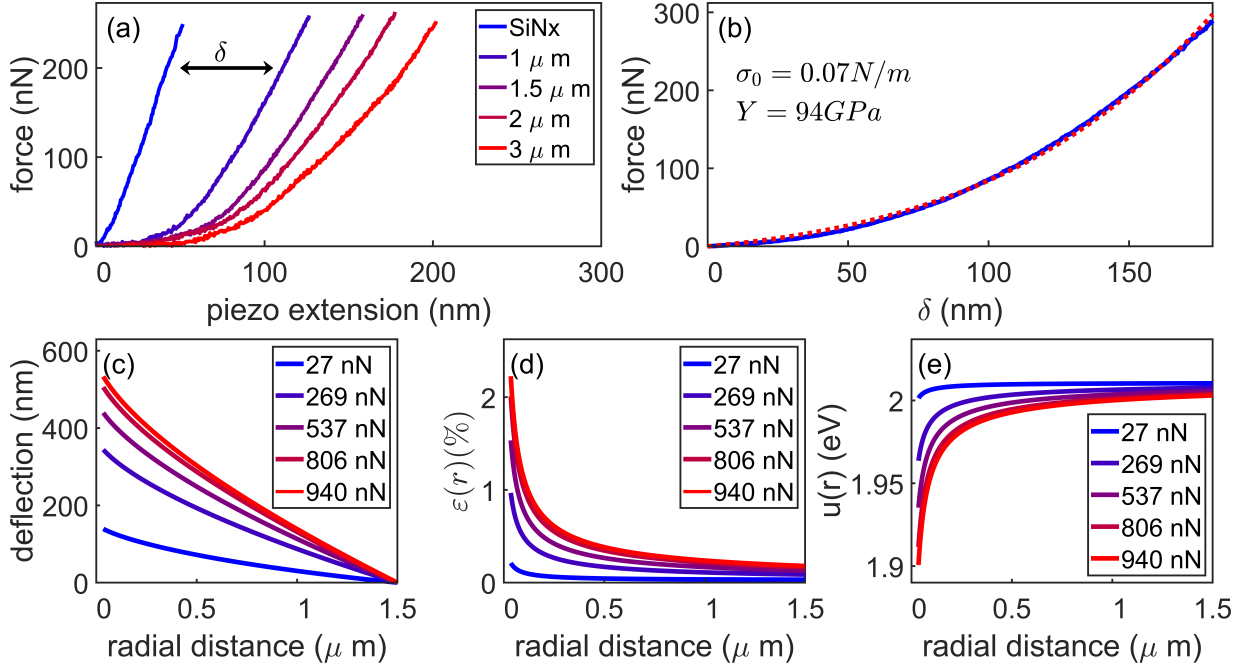


FIG. S2 (a) Force-distance curves of nanindentation experiments on SiNx (blue curve) and WS₂ monolayers suspended on holes with different diameters. The deflection δ is defined as the difference between the SiNx deflection and the deflection of the investigated WS₂. (b) Fitting the force-distance curve for the data of the 3 μm diameter hole from (a). The fit is done with the method given in Ref. S3 and the elastic properties of the monolayer are extracted. Using the extracted elastic properties, we can calculate the deflection of the membrane for different AFM tip forces (c), the total strain distribution (d) and the band-gap (e). Note that the calculations are valid only from the AFM tip radius and on, as discussed in the main text.

the strain profile, we took the approach from Ref. S3 which proved to be the most accurate way to extract the experimental strain profile.

The first step was to perform a nanindentation experiment using a commercial AFM (Bruker JPK NanoWizard4)^{S4,S5}. This is shown in Fig. S2(a) for sample A. Similar data was also acquired for samples B and C. In this experiment we show the force-distance curve for the SiNx membrane and suspended WS₂ flakes on top of holes with different diameters. The deflection δ of the middle point of the suspended WS₂ measured with respect to SiNx is extracted and fitted using the procedure developed in Ref. S3 (Fig. S2(b)). The fitted force-distance curve is crucial for extracting the correct elastic properties (pre-tension σ_0 and Young's modulus Y) of the individual suspended monolayer as they can vary between samples. The Young's modulus obtained from the analysis of Ref. S3 deviates from the value of 208 GPa obtained for the same data using the more standard cubic fit analysis. However, either value results in almost equivalent strain distribution and derived quantities. Using the extracted elastic properties, we calculate the deflection of the membrane (Fig. S2(c)), the total strain $\varepsilon(r)$ (Fig. S2(d)), and the band-gap $u(r)$ (Fig. S2(e)) for different experimental forces of the AFM tip. The band-gap is calculated as:

$$u(r) = E_g - 0.05 \cdot \varepsilon(r) \quad (\text{S1})$$

where E_g is the band-gap value at zero strain. The decrease of the band-gap for WS₂ is 50 $\text{meV}/\%$ ^{S6,S7}, and $\varepsilon(r) = \varepsilon_{rr}(r) + \varepsilon_{\theta\theta}(r)$ are the radial and angular strain tensor components that are calculated directly using the method described above. As the calculation is valid only in the region $r_{tip} < r < r_{membrane}$ (where r_{tip} ($r_{membrane}$) is the AFM tip radius (membrane radius), respectively), we assume that the bandgap does not change for $r > r_{membrane}$ and is constant with the value of ε_{max} at $r < r_{tip}$:

$$u(r) = \begin{cases} E_g - 0.05 \cdot \varepsilon(r_{tip}) & r \leq r_{tip} \\ E_g - 0.05 \cdot \varepsilon(r) & r_{tip} < r < r_{membrane} \\ E_g & r > r_{membrane} \end{cases} \quad (\text{S2})$$

We note that the samples broke at different strain magnitudes - sample A at $\varepsilon_{max} \simeq 2.4\%$, sample B at $\varepsilon_{max} \simeq 2.6\%$, and sample C at $\varepsilon_{max} \simeq 3.5\%$.

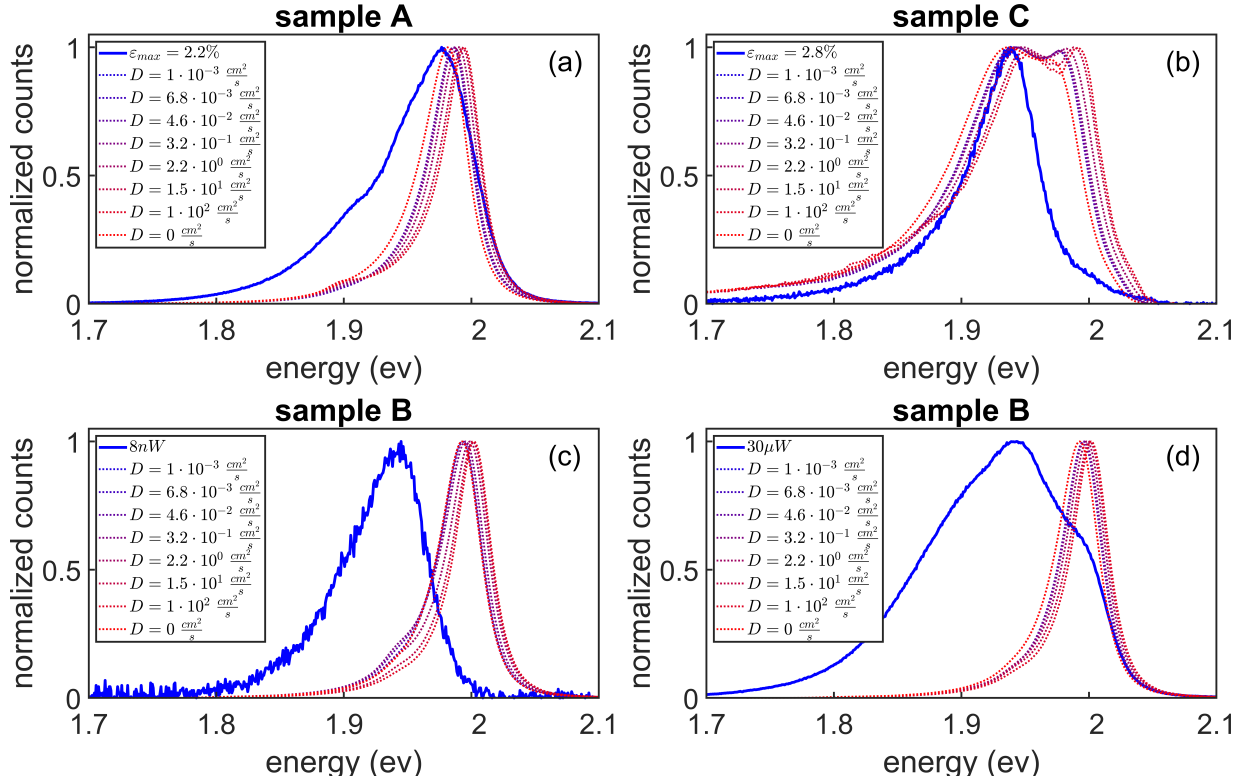


FIG. S3 Calculation of the model with only funneling of carriers and without any exciton to trion conversion for different diffusion coefficients. (a) Sample A, highest experimental strain value. (b) Sample C, highest experimental strain value. (c)-(d) Sample B for low (c) and high (d) laser excitation intensities.

III. DRIFT DIFFUSION WITHOUT TRION CONTRIBUTION

The diffusion-drift equation presented in the main text was solved numerically using the PDE module in Comsol Multiphysics™. The convergence of the solution was verified and compared to simple cases such as no Auger recombination ($R_A = 0$) and no diffusion ($D = 0$). The PL spectrum of WS₂ under strain is calculated as:

$$\langle PL \rangle = \int_0^\infty [PL(u(r))n(r)] r dr \quad (S3)$$

where $n(r)$ is the solution of the diffusion-drift equation and $PL(u(r))$ is the PL spectrum at zero strain, shifted by the energy shift induced by the local strain. In Fig. S3 we present the calculations of Eq. S3 for different diffusion coefficients for all samples. It is easy to observe that the results do not change drastically although the diffusion coefficient spans over 5 (!) order of magnitude. This justifies the use of a single diffusion coefficient in the full model that includes trions and excitons as even though they most probably possess different diffusion coefficients, their spatial distributions will not be altered much.

The funneling efficiency is rather low as described in the main text. Figure S4 presents the different normalized densities as shown also in Fig. 4(c) in the main text. We see that although the density $n(r)$ peaks at the funnel area ($r < r_{tip}$) it still does not contribute much in the area dominated by the integrand (red shaded area).

We calculate the funneling efficiency as:

$$eff = \frac{\int_0^{r_{tip}} n(r) r dr}{\int_0^{r_{membrane}} n(r) r dr} \quad (S4)$$

Figure S5 shows the funneling efficiency for the various samples for various strain magnitude, various intensities, and different diffusion coefficients. We observe that the funneling efficiency peaks for a certain diffusion coefficient. The ideal diffusion coefficient can be found in sample B by looking at the low intensity curve which means negligible Auger recombination (blue curve in Fig. S5(b)) It peaks at a diffusion coefficient slightly lower than the reported value of $D = 0.3 \text{ cm}^2/\text{s}$, measured in Ref. S8. We also observe that the funneling efficiency increases as a function of strain but unfortunately, all samples rupture for strain higher than 2.5% which limits the funneling efficiency.

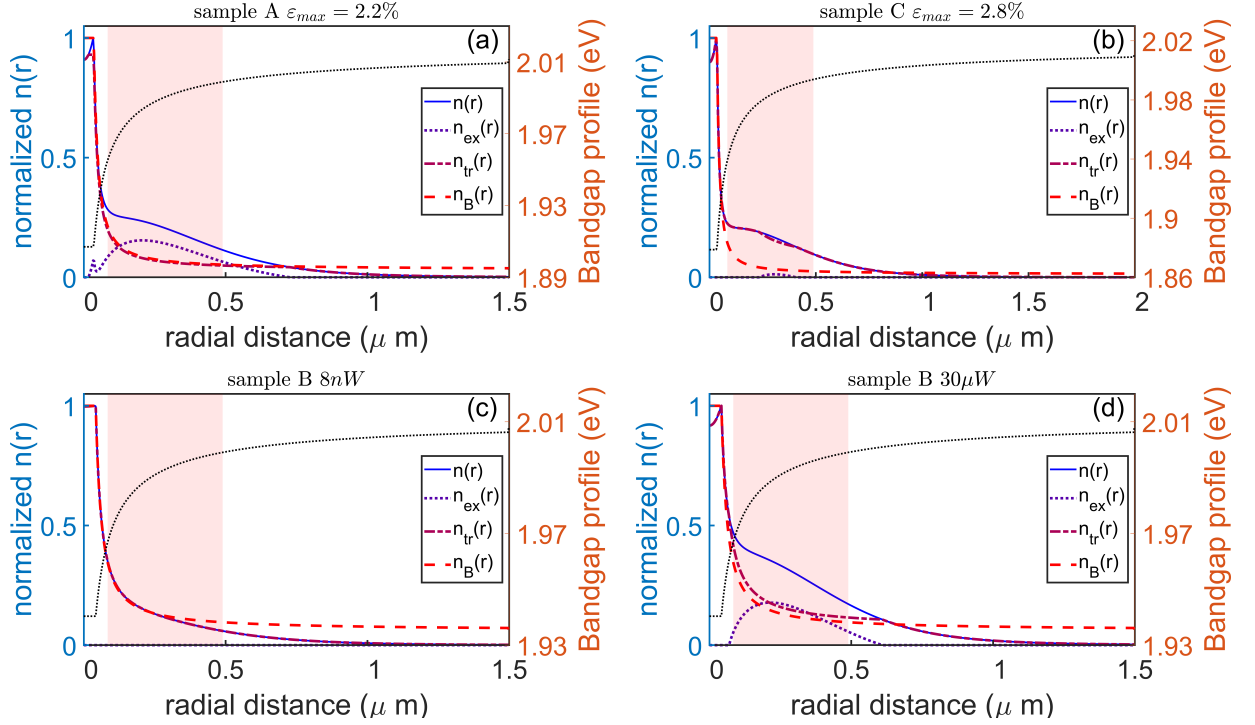


FIG. S4 Carrier density profiles calculated from the model for $D = 0.3 \text{ cm}^2/\text{s}$ with the band-gap profile (black dashed curve). The shaded area represents the dominant contribution to the integrand. (a) Sample A (shown also in the main text). (b) Sample C. (c)-(d) Low (c) and high (d) laser excitation intensity of sample B.

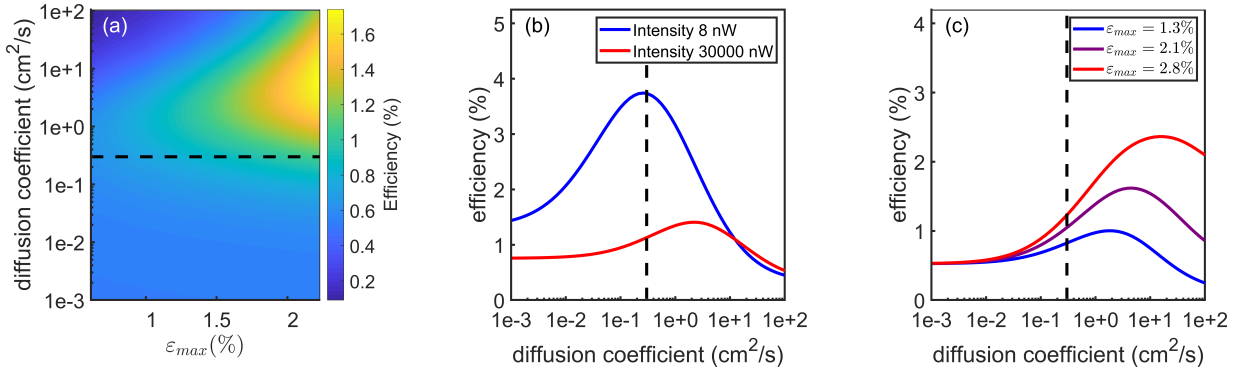


FIG. S5 The funneling efficiency calculated using Eq. S4. Black dashed lines represent the calculation for $D = 0.3 \text{ cm}^2/\text{s}$. (a) The efficiency of sample A (colorbar scale for the efficiency) as a function of maximal strain ε_{max} and diffusion coefficient. (b) Sample B for low (blue curve) and high (red curve) intensity. The efficiency peaks at a diffusion coefficient close to the reported value. (c) Sample C. Shows similar behaviour to sample A.

IV. SPATIALLY DEPENDENT FREE CARRIER DENSITY

In this section we introduce a model for the calculation of the spatial dependence of the free carriers density $n_B(r)$ both for electrons and holes (depending on intrinsic doping level of the sample). The main assumptions of the model are that the contribution to the doping comes from defects with energy levels inside the band-gap, and these energy levels do not change (or at least change very slowly compared to the band-structure^{S9}) due to strain. In this approximation, we start by looking at the diffusion-drift equation presented in the main text. In the case of free carriers, there is no generation of free carriers ($S(r) = 0$), no lifetime term, and no Auger recombination. This reduced the diffusion-drift equation to:

$$D\nabla n_B^{c,v}(r) + \mu n_B^{c,v}(r)\nabla u_{c,v}(r) = 0 \quad (\text{S5})$$

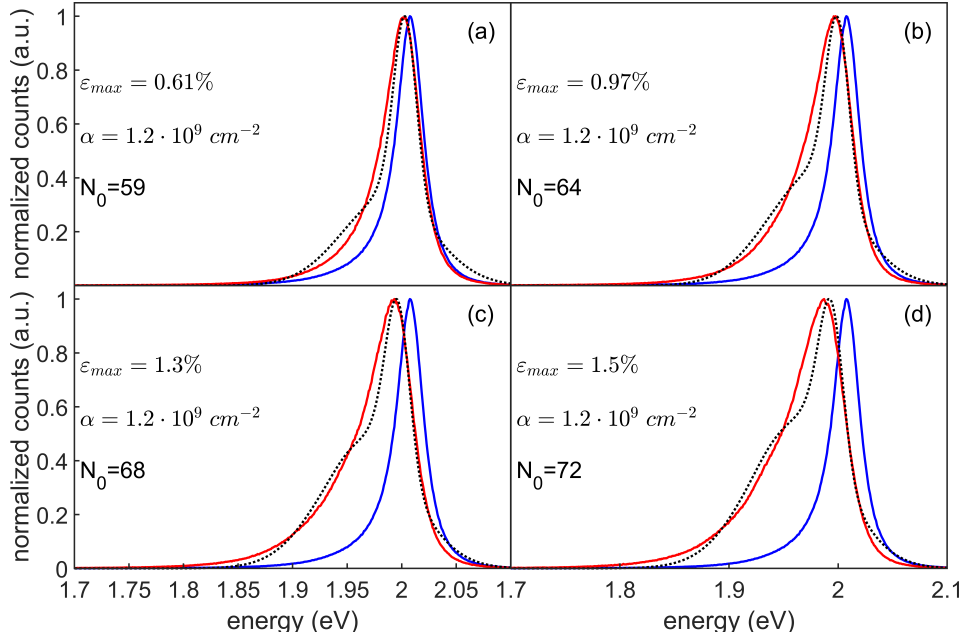


FIG. S6 (a)-(d) Different strain magnitudes for sample A with the normalized spectra at zero strain (blue curve), at the center of the membrane (red solid curve), and the full model with the trion conversion (black dashed line). Note that N_0 increases as a function of strain but α remains constant, thus fulfilling the requirement for constant defect density.

where $u_c(u_v)$ is the change in the conduction (valence) band for electrons (holes), respectively. The exact solution of Eq. S5 is:

$$n_B^{c,v}(r) = \frac{N_0 e^{-\beta u_{c,v}(r)}}{\int e^{-\beta u_{c,v}(r)} r dr} \quad (\text{S6})$$

where $\beta = 1/k_B T$ comes from the Einstein relations $\frac{\mu}{D} = \beta$, and $\frac{N_0}{\int e^{-\beta u_{c,v}(r)} r dr}$ is an integration constant. We relate the integration constant to the global defect density α :

$$\alpha = \frac{N_0}{\int e^{-\beta u_{c,v}(r)} r dr} \quad (\text{S7})$$

75 We emphasize that α is constant due to our assumption of small change of the defect states compared to the WS₂ band-structure. Figure S6 shows different spectra of sample A that are fitted using the same α , thus preserving the same defect density. Going back to the definition of $u_{c,v}$ we can see^{S10} that $u_c(r) = u_c^0 - 0.8 \cdot \Delta u(r) \equiv u_c^0 - \Delta u_c(r)$ and $u_v(r) = u_v^0 + 0.2 \cdot \Delta u(r) \equiv u_v^0 + \Delta u_v(r)$ where $\Delta u(r) = 0.05 \varepsilon(r)$ and $u_{c,v}^0$ is the zero strain value of the conduction (valence) band. Note the different signs for the electrons and the holes^{S11} - electrons concentrated at the center of the funnel while holes are depleted from the funnel region. As our sample is n-doped, the expression for the free carriers
80 reduces to $n_B(r) = \frac{N_0 e^{\beta \Delta u_c(r)}}{\int e^{\beta \Delta u_c(r)} r dr}$ as given in the main text.

Once we have derived an analytical expression to the spatial distribution of $n_B(r)$, we can calculate the 2 relevant densities $n_{ex}(r), n_{tr}(r)$ using the law of mass action^{S12,S13}:

$$n_{tr}(r) = \frac{n(r) + n_B(r) + n_A(r) - \sqrt{(n(r) + n_B(r) + n_A(r))^2 - 4n(r)n_B(r)}}{2} \quad (\text{S8})$$

where $n(r)$ is the diffusion-drift equation solution (Eq. 1 in the main text), and $n_A(r) = \frac{4m_{ex}m_e}{\pi \hbar^2 m_{tr}} k_B T e^{-\frac{E_T}{k_B T}}$. For
85 WS₂, $m_{tr} = m_{ho} + 2m_{el}$, $m_{ex} = m_{ho} + m_{el}$, $m_{el} = 0.31 m_e$, and $m_{ho} = 0.42 m_e$ with m_e as the electron rest mass. Once we solve Eq. S8, the exciton density is evaluated by $n_{ex}(r) = n(r) - n_{tr}(r)$. Figure S4 shows the spatial dependence at n_{ex}, n_{tr}, n_b , and $n(r)$.

V. DERIVATION OF EQUATION 2 IN THE MAIN TEXT

In the main text we give an argument about the efficiency of funneling using Eq. 2. The argument begins by
90 looking at the drift and diffusion currents:

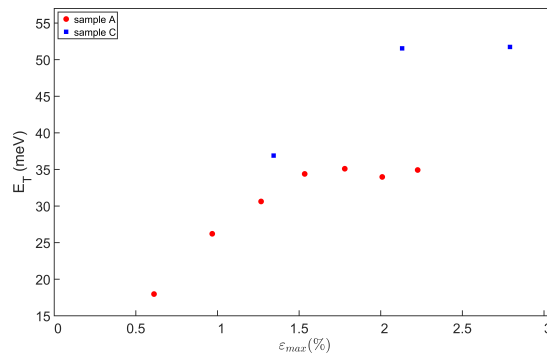


FIG. S7 The trion binding energy as a function of the maximal strain ε_{max} . The red circles (blue squares) correspond to sample A (C), respectively.

$$\vec{J}_D = D\nabla n(r) \quad (S9)$$

$$\vec{J}_\mu = \mu n(r)\nabla u(r) \quad (S10)$$

Which one of the currents is more dominant? The ratio of \vec{J}_D/\vec{J}_μ leads to the following inequality:

$$D\nabla n(r) + \mu n(r)\nabla u(r) < 0 \Rightarrow k_B T < -\frac{n(r)\nabla u(r)}{\nabla n(r)} \quad (S11)$$

where we used the Einstein relations $\frac{D}{\mu} = k_B T$. To evaluate Eq. S11 we use the following assumption - the laser is turned on at time $t=0$ and shuts down immediately, thus the distribution is $n(r) = S(r)$ as at time $t=0$. This distribution gives us Eq. 2 in the main text.

VI. TRION BINDING ENERGY

Trion binding energy was used as a fit parameter to take into account the increase of the trion density. Indeed, it has been observed that the trion binding energy increases as a function of trion density^{S14,S15}. As we have seen in the main text that the contribution to the spectrum comes from a rather small area outside the funnel, we can take E_T to be spatially independent. In Fig. S7 we show the trion binding energy, which was obtained by fitting the spectra of samples A and C (Fig. 1(a),(c) in the main text), as a function of increasing strain. Sample A (red circles) shows a saturation behaviour, most probably due to low defect density. Sample C (red squares) shows higher binding energies due to higher defect density compared to sample A, but it also saturates at large strain values.

To evaluate if the increase in the trion binding energy fits our model, we calculate the effective free carrier density from averaging $n_b(r)$ over the laser excitation spot. Another method to calculate the free carrier density is by using the energy difference of the trions and excitons. Using the method presented in Ref. S14 we can calculate the free carrier density as:

$$n_b = \frac{2m_e E_F}{\pi \hbar^2} \quad (S12)$$

where $E_F = E_X - E_T - E_{bind}$ is the Fermi energy and E_{bind} as the trion binding energy in undoped WS₂. We show both calculations in Fig. S8. For sample A we see that our model (black triangles) shows that the free carriers density increases as we apply more strain as explained in the main text. The calculation based on Ref. S14 also shows increase in the free carrier density. We see the same behaviour in sample C (our model - blue downward triangles; trion and exciton energy difference - blue pentagons).

VII. POWER DEPENDENCE

The PL power dependence was measured at zero strain as presented in Fig. S9. Firstly, we cannot observe any trion emission. Secondly, it is clear that there is increase in the red tail of the PL emission line. This has been studied^{S7,S16} and has been identified as phonon-assisted broadening which in the case of WS₂ shows an enhanced red tail as a function excitation power. We note that under strain it has been shown that the red tail does not change in WS₂^{S7}.

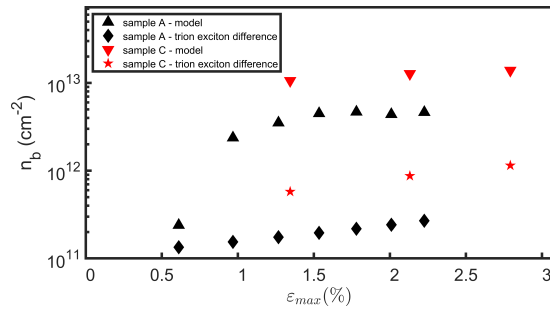


FIG. S8 Calculations of the effective free carrier density n_b for sample A are shown as black triangles (diamonds) for calculations based on our model (trion exciton difference^{S14}), respectively. Similar calculations for sample C are presented as red downward triangles (pentagons), respectively.

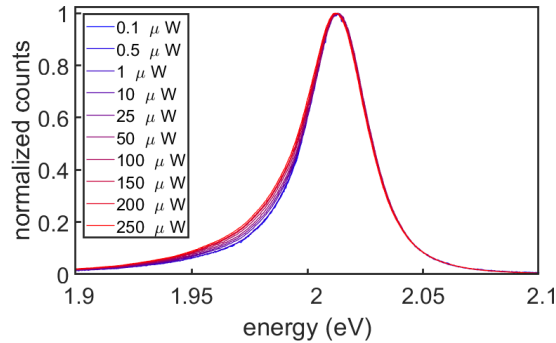


FIG. S9 The normalized PL emission from an unstrained suspended WS₂ monolayer as a function of laser excitation power. The only difference between the spectra is monotonic increase of the red tail as explained in the text.

VIII. AREA SCANS

In order to find the point of maximum strain, we performed area scans using our optical periscope setup (see section I). Figure S10(a),(c) shows such area scans for samples A and C, respectively. Using these area scans, we find the point of maximum strain (the point of indentation) by finding the spectrum which is most red-shifted (numbered as #1 in Fig. S10). In addition, we present the optical spectra taken for excitation of the sample at increasing distance from the point of maximum strain. Our model predicts that as we excite further away from the center of the indentation, the conversion from exciton to trions should decrease as the reduction in the conduction band decreases. This is shown in Fig. S10(b),(d) for sample A and C, respectively.

As explained in the main text, we recorded the spectra during spatial scans across the sample (100 nm spatial resolution). The spectra were fitted to two emission lines - a Gaussian line for the exciton and a modified Gaussian for the trion to account for the electron recoil effect^{S17}. This analysis was done also for sample B for the high intensity excitation and is presented in Fig. S11. We can see that indeed the trion emission is enhanced at the center of the membrane as shown for sample A in the main text.

A representative fit for the spectrum under strain is shown in Fig. S12. The fit quality is surprisingly high, as one would expect to see asymmetric broadening of the emission lines, resulting from averaging the PL over a non-uniform strained profile. This is avoided due to the fact that most of the emission comes from $\simeq 250$ nm from the center of the membrane as explained in the main text. In this region, the strain is rather constant which means that in fact we barely average over different strain values. This allows a very good fit to the spatially dependent spectra.

^a)Electronic mail: bolotin@fu-berlin.de

[S1]A. Castellanos-Gomez, M. Buscema, R. Molenaar, V. Singh, L. Janssen, H. S. J. van der Zant, and G. A. Steele, “Deterministic transfer of two-dimensional materials by all-dry viscoelastic stamping,” *2D Materials* **1**, 011002 (2014).

[S2]M. Dukic, J. D. Adams, and G. E. Fantner, “Piezoresistive AFM cantilevers surpassing standard optical beam deflection in low noise topography imaging,” *Scientific Reports* **5**, 16393 (2015).

[S3]D. Vella and B. Davidovitch, “Indentation metrology of clamped, ultra-thin elastic sheets,” *Soft Matter* **13**, 2264–2278 (2017).

[S4]A. Castellanos-Gomez, M. Poot, G. A. Steele, H. S. J. van der Zant, N. Agrait, and G. Rubio-Bollinger, “Elastic Properties of Freely Suspended MoS₂ Nanosheets,” *Advanced Materials* **24**, 772–775 (2012).

[S5]R. Zhang, V. Koutsos, and R. Cheung, “Elastic properties of suspended multilayer WSe₂,” *Applied Physics Letters* **108**, 042104 (2016).

[S6]H. J. Conley, B. Wang, J. I. Ziegler, R. F. Haglund, S. T. Pantelides, and K. I. Bolotin, “Bandgap Engineering of Strained Monolayer and Bilayer MoS₂,” *Nano Letters* **13**, 3626–3630 (2013).

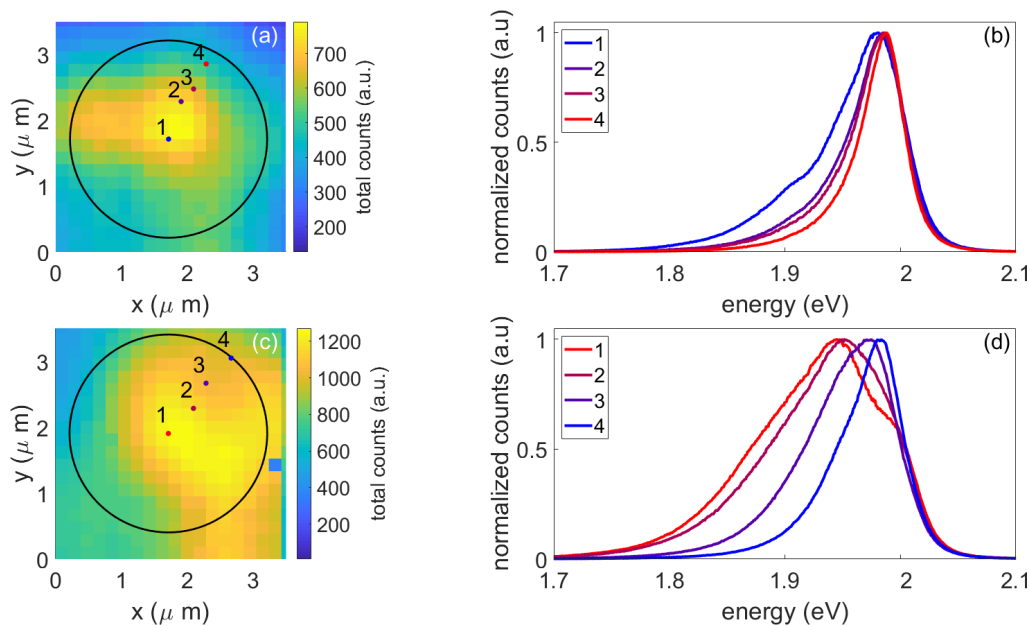


FIG. S10 (a) An area scan of the total PL counts from sample A for the highest strain value of $\epsilon_{max} = 2.2\%$. The numbers note the location of the different spectra shown in (b), where we can observe slight blue shift and decrease of the trion peak as we go further away from the point of indentation. (c)-(d) Same data for sample C for $\epsilon_{max} = 2.8\%$.

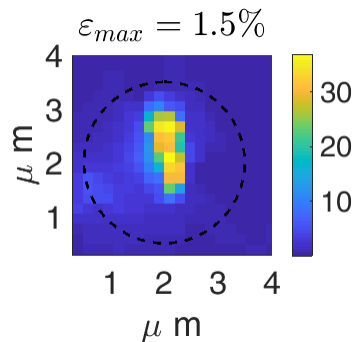


FIG. S11 A spatial map of the trion-to-exciton ratio of sample B for high excitation power. In this sample the conversion efficiency is much higher than from sample A and exceeds 30.

- [S7]I. Niehues, R. Schmidt, M. Drüppel, P. Marauhn, D. Christiansen, M. Selig, G. Berghäuser, D. Wigger, R. Schneider, L. Braasch, R. Koch, A. Castellanos-Gomez, T. Kuhn, A. Knorr, E. Malic, M. Rohlfing, S. Michaelis de Vasconcellos, and R. Bratschitsch, “Strain Control of ExcitonPhonon Coupling in Atomically Thin Semiconductors,” *Nano Letters* **18**, 1751–1757 (2018).
- [S8]M. Kulig, J. Zipfel, P. Nagler, S. Blanter, C. Schüller, T. Korn, N. Paradiso, M. M. Glazov, and A. Chernikov, “Exciton Diffusion and Halo Effects in Monolayer Semiconductors,” *Physical Review Letters* **120**, 207401 (2018).
- [S9]C. Kittel, *Introduction to solid state physics* (Wiley, 2005) p. 680.
- [S10]H. Shi, H. Pan, Y.-W. Zhang, and B. I. Yakobson, “Quasiparticle band structures and optical properties of strained monolayer MoS₂ and WS₂,” *PHYSICAL REVIEW B* **87**, 155304 (2013).
- [S11]J. Feng, X. Qian, C.-W. Huang, and J. Li, “Strain-engineered artificial atom as a broad-spectrum solar energy funnel,” *Nature Photonics* **6**, 866–872 (2012).
- [S12]J. Siviniant, D. Scalbert, A. V. Kavokin, D. Coquillat, and J.-P. Lascaray, “Chemical equilibrium between excitons, electrons, and negatively charged excitons in semiconductor quantum wells,” *Physical Review B* **59**, 1602–1604 (1999).
- [S13]J. S. Ross, S. Wu, H. Yu, N. J. Ghimire, A. M. Jones, G. Aivazian, J. Yan, D. G. Mandrus, D. Xiao, W. Yao, and X. Xu, “Electrical control of neutral and charged excitons in a monolayer semiconductor,” *Nature Communications* **4**, 1474 (2013).
- [S14]K. F. Mak, K. He, C. Lee, G. H. Lee, J. Hone, T. F. Heinz, and J. Shan, “Tightly bound trions in monolayer MoS₂,” *Nature Materials* **12**, 207–211 (2013).
- [S15]B. Zhu, X. Chen, and X. Cui, “Exciton Binding Energy of Monolayer WS₂,” *Scientific Reports* **5**, 9218 (2015).
- [S16]D. Christiansen, M. Selig, G. Berghäuser, R. Schmidt, I. Niehues, R. Schneider, A. Arora, S. M. de Vasconcellos, R. Bratschitsch, E. Malic, and A. Knorr, “Phonon Sidebands in Monolayer Transition Metal Dichalcogenides,” *Physical Review Letters* **119**, 187402 (2017).
- [S17]G. Plechinger, P. Nagler, J. Kraus, N. Paradiso, C. Strunk, C. Schüller, and T. Korn, “Identification of excitons, trions and biexcitons in single-layer WS₂,” *Physica Status Solidi - Rapid Research Letters* **9**, 457–461 (2015).

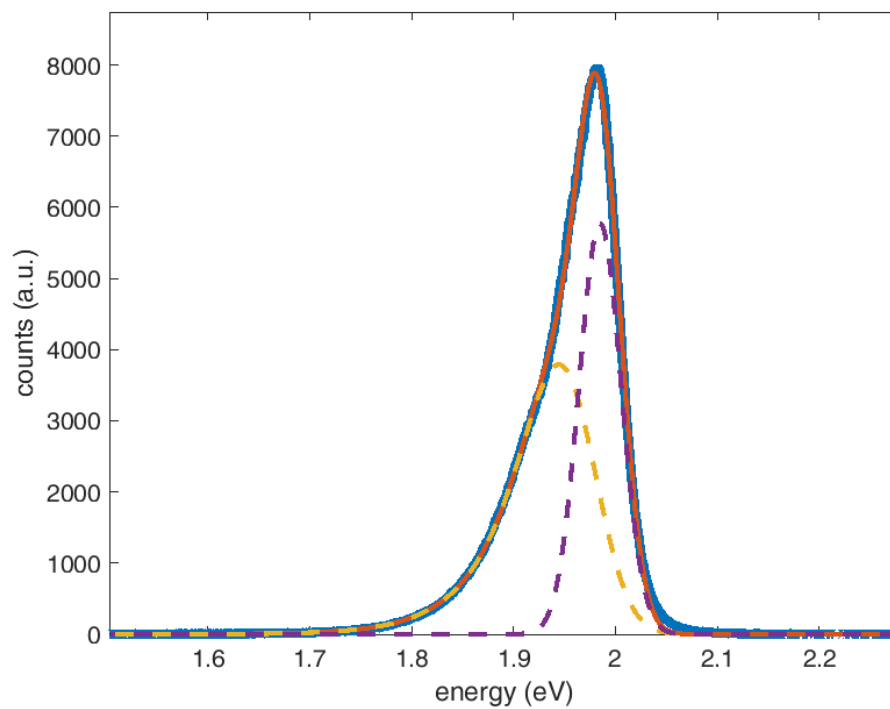


FIG. S12 A representative fit of a spectrum taken from the highest strain in sample A area scan. The blue curve corresponds to the experimental spectrum and the red curve is the fit to the trion and exciton emission lines. The dashed yellow (purple) curves show the individual emission lines for the trion (exciton), respectively.